Toxicity evaluations of nanoclays and thermally degraded byproducts through spectroscopical and microscopical approaches

Alixandra Wagner[a], **Reem Eldawud**[a], **Andrew White**[a], **Sushant Agarwal**[a], **Todd A. Stueckle**[b], **Konstantinos A. Sierros**[c], **Yon Rojanasakul**[d], **Rakesh K. Gupta**[a,*], and **Cerasela Zoica Dinu**[a,*]

[a]Department of Chemical and Biomedical Engineering, West Virginia University, Morgantown, WV 26506, USA

[b]National Institute for Occupational Safety and Health, Morgantown, WV 26505, USA

[c]Department of Mechanical and Aerospace Engineering, West Virginia University, Morgantown, WV 26506, USA

[d]Department of Pharmaceutical Sciences, West Virginia University, Morgantown, WV, 26506, USA

Abstract

Background—Montmorillonite is a type of nanoclay that originates from the clay fraction of the soil and is incorporated into polymers to form nanocomposites with enhanced mechanical strength, barrier, and flammability properties used for food packaging, automotive, and medical devices. However, with implementation in such consumer applications, the interaction of montmorillonite-based composites or derived byproducts with biological systems needs to be investigated.

Methods—Herein we examined the potential of Cloisite Na$^+$ (pristine) and Cloisite 30B (organically modified montmorillonite nanoclay) and their thermally degraded byproducts' to induce toxicity in model human lung epithelial cells. The experimental set-up mimicked biological exposure in manufacturing and disposal areas and employed cellular treatments with occupationally relevant doses of nanoclays previously characterized using spectroscopical and microscopical approaches. For nanoclay-cellular interactions and for cellular analyses respectively, biosensorial-based analytical platforms were used, with induced cellular changes being confirmed via live cell counts, viability assays, and cell imaging.

[*]Corresponding authors at: Department of Chemical and Biomedical Engineering, West Virginia University, Benjamin M. Statler College of Engineering and Mineral Resources, PO Box 6102, Morgantown, WV 26506, USA. rakesh.gupta@mail.wvu.edu (R.K. Gupta), cerasela-zoica.dinu@mail.wvu.edu (C.Z. Dinu).

Results—Our analysis of byproducts' chemical and physical properties revealed both structural and functional changes. Real-time high throughput analyses of exposed cellular systems confirmed that nanoclay induced significant toxic effects, with Cloisite 30B showing time-dependent decreases in live cell count and cellular viability relative to control and pristine nanoclay, respectively. Byproducts produced less toxic effects; all treatments caused alterations in the cell morphology upon exposure.

Conclusions—Our morphological, behavioral, and viability cellular changes show that nanoclays have the potential to produce toxic effects when used both in manufacturing or disposal environments.

General significance—The reported toxicological mechanisms prove the extensibility of a biosensorial-based platform for cellular behavior analysis upon treatment with a variety of nanomaterials.

Keywords

Nanoclay; Lung cell; Toxicity; Thermal degradation; Montmorillonite; Byproduct

1. Introduction

Nanotechnology is quickly establishing itself as the next revolution in commercial and industrial products, with about one third of all produced engineered nanomaterials to occur within the U.S. [1,2]. Naturally occurring montmorillonite nanoclays [3,4] are readily available, negatively charged [5], low cost [6], and consist of aluminum or magnesium octahedral sheets sandwiched between two silica-oxygen tetrahedral sheets. Isolated from the clay fraction of the soil [7], nanoclays are currently used as sorbents in the treatment of waste water or hazardous spills [8], or as media for oil well drilling [9], paints [10], and cosmetics [11]. Functionalization with organic modifiers via an ion exchange reaction confers montmorillonite increased basal spacing and separation between its platelets [4,12] as well as better mixing ability, and facilitates its interactions with hydrophobic polymers [3,4,13]. Complementary, its high aspect ratio [5] ensures better reinforcement within the polymeric plane itself [14] by enhancing polymer's properties at a fairly low silicate content [13] and leading to the formation of nanoclay-polymer-based composites with increased mechanical strength [3,14], barrier properties [3,15], UV dispersion [15], and fire resistance capabilities [3,16], to be used for food packaging [17,18], automotive [19,20], medical devices [21,22], and for coatings-related applications [23,24].

With nanoclay or nanoclay-plastic composites wide implementation [25], analyses of potential risks of these nanomaterials to exposed workers lung's health have started to emerge. As such, recent studies aiming to unravel the nanoclay toxicological profiles showed that its high aspect ratio resulted from its platelet thickness of about 1 nm and length and width of up to several microns [5], has led to increased cellular uptake and interactions [26]. While such *in vitro* analyses allowed for elimination of animal subjects, lower processing time, and cost effectiveness [27,28], they rely on usage of synthetic compounds such as tetrazolium salts (MTT) to measure mitochondrial reduction/cellular viability for instance [28]. Specific results based on such analyses revealed that cellular exposure to

nanoclays lead to mitochondrial damage [29–31], decreased cellular proliferation [32], reactive oxygen species (ROS) generation [29,31], as well as membrane [29,33] and DNA damage [30,34,35], with the type and range of toxicity being dependent on the cell model being used, the dosage, and the organic modifier functionalizing the nanoclay, respectively [5]. However, based on our knowledge no analyses are currently available to report the toxicological profiles of nanoclays upon the end of composite life cycle [26,36]. High temperatures, oxidation, reduction, and potential chemical reactions occurring during the incineration process normally used for composites disposal [37] could induce physical and chemical changes [38] and lead to increased reactivities of the resulting nanoclay-resulting byproducts. Further, previous analyses on other types of nanomaterials have showed that single-walled carbon nanotubes (SWCNTs), carbon black nanoparticles, fullerenes, and silica for instance, all interact with indicator dyes such as the MTT by binding to the formazan crystals and making them insoluble and thus creating false positives [27,39,40]. Additionally, the high adsorptive capacities of nanomaterials due to their large surface per unit mass have shown interferences with annexin V/PI binding, ELISA, and ROS assays [27, 28]. Finally, Casey et al. found considerable variation in the toxicity of carbon nanomaterials on human alveolar carcinoma cells (A549) from MTT, Commassie Blue, Neutral Red, and WST-1 assays, all of which help indicate cellular viability [41].

Given the complex effects of nanoclays on increased cellular instability, previous research showing possible interference between nanomaterials in general and the assays being used, and lastly, given that smaller particles resulting from incineration are more likely to escape filters [37] and travel greater distances through the air by Brownian diffusion [26] leading to deeper inhalation, larger sedimentation and diffusion rates into the lungs [26,42], it is important that we perform a systemic analysis to assess how parallel exposures to nanoclay or byproducts resulted during their manipulation, handling, and disposal affects cellular systems' fate. Such tests should be cheap, not time intensive [43] or invasive [43], and provide results in real-time in contrast with discrete time points currently achieved through the standard assays named above [44,45]. Further, such assays should be high throughput and should have the ability to provide accurate evaluations that avoid the artifacts known to result from the interaction of nanomaterials with dyes or chemical compounds normally found in standard assays [39–41].

Herein we propose to assess toxicological profiles of nanoclays, both during the duration as well as at the end of their life cycle. Further, to eliminate the concern associated with using standardized single point assays and chemical compounds interference, we propose to use an electrical cell-substrate impedance sensing (ECIS) previously applied to monitor changes in cell adherence, proliferation, motility, and morphology. Our analyses will allow quantitative measurements, at a nanoscale resolution, and in a noninvasive, real-time manner [44–47] to establish whether nanoclays and their thermally degraded byproducts are leading to cellular changes when exposed to model target inhalation systems at an occupationally relevant dose for particles otherwise not regulated [48,49]. Exploitation of our findings can further advance implementation of nanoclays or nanoclay-polymer-based composites in "safe-by-design" consumer-based applications, as well as confirm that ECIS has the potential to be a powerful tool for quickly, efficiently, and non-invasively determining toxicity of a large variety of nanomaterials.

2. Experimental

2.1. Nanoclay preparation

Raw (as received) Cloisite Na⁺ (UC) and Cloisite 30B (CC) were obtained from Southern Clay Products (Gonzales). Cloisite Na⁺ is an unmodified montmorillonite while Cloisite 30B is organically modified via an ion-exchange reaction (per the manufacturer specifications) with methyl, tallow, bis-2-hydroxyethyl, quaternary ammonium at a concentration of 90 meq/100 g clay [4,5].

2.2. Thermal degradation

UC and CC samples were thermally degraded using a TGA701 Thermogravimetric Analyzer from LECO to mimic the end of life cycle. In order to determine the moisture content of the samples, around 0.5 g of each of the samples was heated in nitrogen at a rate of 6 °C/min and in a range of temperatures from 25 °C to 105 °C. To determine the volatile content, the samples were heated from 105 °C to 950 °C in nitrogen at a rate of 43 °C/min. Finally, to determine the ash content, the samples were heated from 550 °C to 900 °C in oxygen at a rate of 15 °C/min. The resulted ash was collected to serve as a model of the byproducts resulted from incineration i.e., thermally degraded Cloisite Na⁺ (UC900) and thermally degraded Cloisite 30B (CC900), respectively.

2.3. Material characterization

Chemical composition of the samples (i.e., unsterile and sterilized clays, and their thermally degraded byproducts) was determined using Fourier Transform Infrared Spectroscopy (FTIR, Digilab FTS 7000) equipped with diamond Attenuated Total Reflection (ATR). Unsterile and samples sterilized under UV for 30 min were investigated to compare whether the sterilization, otherwise necessary for further biological-based studies, changes the physical and chemical properties of the nanoclays. Scans were collected in the range of 4000–400 cm⁻¹ at a resolution of 4 cm⁻¹; a total of 100 scans were co-added to form the final spectrum for each of the samples.

Surface morphology and elemental composition of the samples were investigated using a Hitachi S-4700 Field Emission Scanning Electron Microscope (SEM, Hitachi High-Technologies Corporation) equipped with an energy dispersive X-ray spectroscopy (EDX). Surface morphology was examined at 5.0 kV while elemental composition was determined at 20.0 kV. For the analyses, dry powder samples were mounted onto a carbon tape and then sputter coated for 10 s in a vacuum injected with argon using a gold/palladium target. The argon atoms were ionized and collided with the gold/palladium target, causing the metal ions to deposit on the sample in a thin conductive layer of about 3 nm as calculated using the equation $d = KIVt$, where d is thickness, k is a constant value of 0.17, I is plasma current, V is voltage, and t is the time.

The size distribution of the samples was determined by dynamic light scattering (DLS) via the Mastersizer 2000 with a Hydro 2000S accessory (Malvern Instruments). For this, solutions of UC, CC, UC900, or CC900 dispersed and bath sonicated in cell culture media (Dulbecco's Modified Eagle Medium: DMEM) containing 5% fetal bovine serum (FBS) or

in phosphate buffered saline (PBS) were dropped into the Hydro 2000S until laser obscuration was within 10–20% (all reagents were purchased from Life Technologies). The size analysis was performed 3 consecutive times with a stirrer speed of 1750 rpm and under continuous sonication.

Samples' sedimentation studies were performed by tracking changes in absorbance upon different incubation times when using an Evolution 300 UV–VIS spectrophotometer (Thermo Scientific). Briefly, concentrations of 100 μg/ml of UC, CC, UC900, and CC900 were prepared in media as described above. The maximum absorbance of each sample was obtained by scanning the absorbance in the 400–1100 nm range. Sedimentation was determined by measuring the changes in absorbance of each solution at the obtained maximum absorbance of 560 nm after 0, 0.5, 1, 2, 3, 4, 5, and 6 h incubation in media respectively, with media serving as the blank at each time point.

2.4. Cell culture

Immortalized human bronchial epithelial cells (BEAS-2B) were cultured in media containing 1% L-glutamine, and 1% penicillin-streptomycin (all reagents were purchased from Life Technologies). The cells were passaged regularly using 0.25% trypsin (Invitrogen) and incubated at 37 °C, 5% CO_2 and 80% relative humidity. Before each experiment cells were grown to a confluent monolayer.

2.5. Electrical cell-substrate impedance testing

Real-time measurements of cellular resistance and attachment were performed using an electrical cell-substrate impedance sensing instrument (ECIS-ZΘ, Applied Biophysics). For the cellular studies, a 96 well plate (96W10idf) that contained inter-digitated finger connection electrodes covering an area of 3.985 mm^2 of each well was used. Before addition of the cells, the electrodes were stabilized for 2 h with 200 μl media to minimize electrode drift during the experiment. After stabilization the cells were added at a density of 1.50E + 05 cells/ml in a volume of 150 μl/well. The cells were allowed to grow for 24 h until they reached a confluent monolayer, as indicated by a constant level resistance [50]. After 24 h, 100 μg/ml of UC, CC, UC900, or CC900 (unsterilized) dispersed in media was added to their respective wells; cells in media served as the control. Subsequently, 24 h after treatment, the media was removed and the cells were washed 2 times with PBS. Fresh media was added to all of the wells, and the recovery of the cells was monitored for 48 h.

2.6. Live cell count

BEAS-2B cells were seeded in a 12 well plate (Thermo Scientific) at a density of 2.0E + 05 cells/ml. After 24 h, the cells were treated with UC, CC, or thermally degraded byproducts at a dose of 100 μg/ml. Before addition to the respective wells, each of the samples was sonicated for 8–10 min in media in a bath sonicator (2510 Branson); cells in only media served as controls. Twenty-four, 48, and 72 h post exposure to UC, CC, or thermally degraded byproducts, the cells were trypsinized and stained with 0.4% trypan blue solution (Invitrogen). Subsequently, 10 μl of the sample containing the stained cells was added to a hemocytometer, and the number of cells in the 4 outer grids was counted through the use of the Leica DM IL optical microscope (Leica Microsystems) using a 10× objective. Analyses

of cellular proliferation after exposure to UC, CC, UC900, and CC900, along with their sterilized counterparts, respectively were performed through direct live cell counts to eliminate concerns associated with false positive as resulted from the similar sizes of the cells and clay suspensions.

2.7. Cellular viability

BEAS-2B cells were seeded in a 96 well plate (Thermo Scientific); 2.0E + 05 cells/ml were used. After 24 h, 100 μg/ml of UC, CC, UC900, or CC900 (unsterilized and sterilized) dispersed in media was added to their respective wells while cells in media served as control samples. The 4-[3-(4-idophenyl)-2-(4-nitrophenyl)-2H-5-tetrazolio]-1,3-benzene disulfonate known as WST-1 assay (Roche) was used to determine cellular viability as a change in color produced when cellular dehydrogenases reduced WST-1 to formazan [51]. The color change is known to be directly correlated with the number of metabolically active cells [51]. Briefly, after 24, 48, and 72 h of exposure, 10 μl of WST was added to the wells. Cells (exposed and control) were incubated for 2.5 h and changes in their absorbances were evaluated using a FLUOstar OPTIMA plate reader (BMG LABTECH) and 485 nm absorbance. Media, UC + media, CC + media, UC900 + media, and CC900 + media (unsterilized and sterilized) served as blanks and resulted absorbance values were subtracted from the cellular measurements counterparts.

2.8. Cell imaging

BEAS-2B cells were seeded on glass coverslips in a 12 well plate at a density of 1.5E + 05 cells/ml overnight. The cells were subsequently exposed to 100 μg/ml of UC, CC, UC900, or CC900 (unsterilized) dispersed in media. After 24 h, the media was removed and the cells were washed two times with Hank's Balanced Salt Solution (HBSS) (Corning), fixed with 4% formaldehyde (Sigma-Aldrich) for 15 min at 37 °C, and subsequently washed 3× with HBSS to remove any remaining formaldehyde. The cells plasma membrane and nuclei were then stained with 3 μg/ml Alexa Fluor 594 wheat germ agglutinin (WGA) and 2 μM Hoechst 33342 (Image-iT LIVE Plasma Membrane and Nuclear Labeling Kit, Life Technologies) in HBSS for 10 min at 4 °C. After incubation, cells were washed 2× with HBSS, mounted on glass coverslips, and imaged under a Nikon Inverted Microscope Eclipse Ti Series using a 40× objective. The NIS-Elements BR 3.1 software was used to define and analyze the size and morphology of cells. Around 75 cells per treatment were considered to allow for 375 cell measurements per replicate; a total of 3 replicates were used.

2.9. Statistical analyses

All cellular experiments were repeated at least 6 times for all samples, with the exception of cell imaging which was repeated 3 times for unsterilized clay samples and ECIS which was repeated 4 times for unsterilized clay samples. All tables are presented as the average value with (±) SD values. All graphs are presented as the mean value of the number of indicated replicates with (±) SE bars. Significance was determined by one- or two-way analysis of variance ANOVA with $p < 0.05^*$ indicating significance; a post-hoc test was also run to identify which groups were different from each other if statistical differences were recorded.

3. Results and discussion

We aimed to investigate the toxicological profiles of as received pristine and organically modified nanoclays and their thermally degraded, end of life cycle byproducts using non-destructive and high throughput real-time electroanalytical approaches [44,46,47]. Cloisite Na+ (UC), a pristine montmorillonite, and Cloisite 30B (CC), an organically modified montmorillonite frequently used in food packaging [17,18] and medical industry [21], were used as testing materials to mimic potential human inhalation exposure during nanocomposites manufacturing and usage, while thermally degraded forms of these nanoclays, i.e., Cloisite Na+ (UC900) and Cloisite 30B (CC900), were used to mimic the municipal solid waste incineration disposal environment generated at the product-based nanoclay end of life cycle.

3.1. Nanoclays and their thermally degraded byproduct characterization

First, to mimic the incineration conditions of pristine (UC) or organically modified nanoclay (CC) and thus generate end of life cycle nanoclay byproducts, thermogravimetric analysis (TGA) was used. Briefly, samples degraded under temperatures ranging from 25 to 950 °C allowed moisture, volatile, fixed carbon content, and ash content identifications (Table 1). If initially UC had a greater weight loss, with about 20% weight loss by 105 °C and 5% more in the 105 to 800 °C temperature range, CC experienced the vast majority of its weight loss (about 30%) in the 105 to 800 °C temperature range (Fig. 1a) [30]. Further, a significant higher volatile and ash content were observed for CC relative to the pristine sample, presumably resulted from the functionalization of CC with methyl, tallow, bis-2-hydroxyethyl, quaternary ammonium (per the manufacturer's specifications).

Differences in chemical composition between UC, CC, and their thermally degraded byproducts were confirmed using Fourier transform infrared spectroscopy (FTIR) and are shown in Fig. 1b. Both clays revealed the characteristic peaks indicative of the Si—O—Si stretching vibration of silicate [29,52] at 1000 cm^{-1} and of the Al—OH—Al deformation of aluminates [29,53] at 900 cm^{-1} respectively, while peak shifting was observed after their thermal degradation. The peak around 840 cm^{-1} was a result of the deformation of the OH linked to Al^{3-} and Mg^{2-} [53] while the peak around 630 cm^{-1} was associated with the out of plane vibration of the Al—O group [54,55]. Complementarily, UC900 had an additional peak around 640 cm^{-1} presumably due to Si—O—Si bending [53] while CC900 no longer retained the peaks normally present in its CC form at 2920, 2850, and 720 cm^{-1} respectively, thus confirming the degradation of the organic modifier [56]. Such peaks were likely resulted from the asymmetric or symmetric stretching of the C—H groups included in methylene groups or alkane rock of CH$_2$ for alkanes with 7 or more carbons, respectively [29,53] as supported from the incorporation of the methyl, tallow, bis-2-hydroxyethyl, quaternary ammonium organic modifier during the nanoclay processing [29,53]. Molecular composition of UC, CC, and their thermally degraded counterparts was not changed after UV sterilization (Supplementary information Fig. S1).

Scanning Electron Microscopy (SEM) allowed surface morphologies analyses of the as received and end of life cycle samples (Fig. 2). Generally, UC appeared to have less layering and smoother edges relative to CC (Fig. 2a, b); similarly, UC900 and CC900 existed in

agglomerated forms however, they displayed a fairly uniform surface with smooth edges for UC900 (Fig. 2c) and a more fragmented surface with platelets jutting out for CC900 (Fig. 2d). The observed changes in morphology from pristine nanoclay to thermally degraded nanoclay could be due to both the dehydroxylation of the crystal lattice structure of montmorillonite that occurs around 700 °C [56] as well as from the presence of the organic modifier which causes an increase in the nanoclay's basal spacing [57] and thus possible differences in the platelet structure breakdown during thermal degradation. UV sterilization did not produce significant changes in the surface morphology of UC, CC, or their thermally degraded byproducts (Supplementary information Fig. S2a–d).

UC and CC differed significantly in their elemental composition as determined by energy dispersive X-ray (EDX) spectroscopy (Fig. 2e). Specifically, CC showed a higher weight percent of carbon and a lower weight percent of sodium, both relative to UC, thus confirming the modification with the organic modifier [58]. After thermal degradation however, the weight percent of carbon decreased significantly for CC900, while the weight percent of magnesium, aluminum, and silicon increased; further, no sodium was observed. Complementarily, no significant differences were observed between the elemental composition of UC and its thermally degraded byproduct, UC900. The lower amount of carbon present in CC900 versus CC, as well as the fact that there was no longer a carbon difference between the two forms of thermally degraded clay is consistent with the previous studies and confirms the loss of the organic modifier after sample thermal degradation [56]. Analyses also showed that the elemental composition of UC, CC, and their thermally degraded counterparts was not affected by UV sterilization (Supplementary information Fig. S2e).

All of the samples displayed size distributions in the micrometer range upon sonication in either cellular media (Table 2) or phosphate buffered saline (PBS; Table 3), indicating that samples formed agglomerates. Agglomerate's size distribution was a function of the sample's chemical signature (Fig. 3), with cell culture media with 5% serum containing appropriate cell growth proteins favoring larger agglomerates formation than PBS alone, likely due to the interactions of the clays with the proteins in the media forming coronas [59,60]. Interestingly, analyses showed that CC displayed smaller diameter sizes in both media and PBS relative to the other three samples, likely due to the presence of the organic modifier (Fig. 3a, c). Contrary, thermally degraded samples of CC900 formed larger conglomerates relative to their non-degraded counterparts presumably due to their reduction of OH contents, with a 35% and 36% increase in size for CC900 in media and PBS, respectively, relative to CC (Fig. 3b, d). Table S1 and S2 and Fig. S3a–d (both in Supplementary information) display particle diameter sizes based upon % volume, with results confirming that while there were a greater number of small sized particles, the larger sized particles were taking up more volume. Sedimentation analysis showed that all of the samples had around 85% or more particles settled by 6 h (Supplementary information Fig. S4), with the samples experiencing the greatest sedimentation within the first 3 h.

The measured clay or thermally degraded byproduct sizes were similar to those found in manufacturing and disposal environments [61]. Specifically, manufacturing workplaces showed particle sizes from around 2.3 nm to 50 μm [62,63]. Further, the fly ash from

incinerators was shown to display particles of size distributions ranging from 1 nm to 1000 μm, with a large fraction of such particles being under 100 μm [37,64,65]. This is in contrast with bottom ash [64,65] which was generally shown to contain larger particles normally ranging from around 250 μm to >8 mm, though the majority of the bottom ash was around 2–8 mm [65].

3.2. Evaluate cellular behavior upon exposure to nanoclays or thermally degraded byproducts

Changes in cell-induced impedance signals were used to evaluate the characteristics of epithelial lung cells before and after exposure to as received pristine, organically modified, and end of life cycle nanoclay byproducts, as well as cellular ability to recover from any potential deleterious effects. Specifically, electric cell-substrate impedance sensing (ECIS) quantified changes in cell-substrate interactions and cell morphology, in real-time and non-invasively, all after exposure of human bronchial epithelial cells (BEAS-2B) to 100 μg/ml doses of the above-characterized samples. ECIS was previously used to monitor the morphology, attachment, and movement of cells [46,47], while BEAS-2Bs were previously used as model systems to mimic inhalation toxicity [66]. Previous studies have showed that the size of particles greatly influences their translocation in biological systems, with particles below 2.5 μm reaching the alveoli [42] and larger ones likely affecting cells in the upper airways [42]. Another study showed that the platelet-shaped particle with a projected area diameter up to 25 μm and thickness up to 0.1 μm is able to be respired and deposited in the lungs [67]. BEAS-2B epithelial cells were shown to serve as the first line of defense when a material is introduced into the human lung by respiration. The dose was chosen to represent a 6-year working lifetime, based on 8 h/day and 50 weeks/year as derived from particle deposition studies in rat lungs or computer modeling involving variables related to particle characteristics and lung characteristics of humans, respectively [49,68].

For analysis, the BEAS-2B cells were seeded onto the ECIS chambers and exposed to clays or end of life cycle clay-based byproducts for 24 h (Fig. 4, Region A and Region B, respectively). To assess cellular recovery after clay or byproduct-based treatment, the clays and byproducts were removed and cellular behavior was recorded in real-time for another 48 h, using 4000 Hz (Fig. 4, Region C). The chosen frequency allows for resistance evaluation without effects on cell's plasma membrane [69]. Further, at this frequency, previous analyses have showed that the impedance is dependent on the cell bodies, whereas at the lower or higher frequencies, parameters such as impedance of the electrode/electrolyte interface or the medium, and the constriction resistance of the working electrode dominate the impedance measurements [70].

Our results showed that the resistance of cells treated with the clay or byproduct dropped when compared to the control (Fig. 4a); in particular, CC showed the greatest drop in resistance, with an almost complete loss after 6 h of treatment (Region B). Upon 24 h of treatment and removal of the clays or end of life cycle byproducts, cells treated with UC, UC900, and CC900 were able to regain/maintain their resistance values (Region C). Further, the trends in resistance were similar for both UC and UC900, and slightly lower for CC900; no regain in resistance was however recorded for cells exposed to CC.

3.3. Mechanisms responsible for nanoclays or thermally degraded byproduct cellular changes

Previous analysis have showed that a drop in resistance could be associated with changes in cell-substrate interactions [71], in cell viability and proliferation [72], or in cell shape as resulted from cell death, since flatter, more spread cells are responsible for higher resistance than rounder or apoptotic cells [46,47]. Complementary, complete loss in resistance was shown to be due to cell death and detachment from the electrode [71].

To evaluate the first, namely whether cells exposed to nanoclays show changes in cell-substrate interactions, we used the ECIS's α parameter which details the current through the ventral surfaces of the cells and electrodes [73] (Fig. 4b). Indeed, while CC showed a complete loss in cell-substrate interaction within the course of the study time, cells treated with UC showed a decrease in α relative to the control cells within Region B, however, after clay removal, they maintained their cell-substrate interaction (Region C). Complementary, UC900 and CC900 had similar α values relative to the control, thus indicating that interactions between the cells and the substrate were maintained; however, resistance was lower for both relative to the control, possibly indicating that changes to the cell morphology had occurred. CC900 also showed an increase in the α parameter within the 48 h post treatment removal (Region C) confirming cell recovery.

To evaluate the second, namely whether changes in resistance are due to decreases in cellular viability and proliferation, we used cellular assays. Indeed, analyses showed that UC and CC displayed significant decreases, with CC causing a time-dependent decrease in cellular proliferation and viability over 72 h of exposure, relative to the control, UC, and the thermally degraded byproducts. Similar results were obtained by Maisanaba et al. who showed decreases in cellular viability in a time dependent manner at doses above 3.91 μg/ml upon treatment with CC of the human colon cell line, Caco-2 [31]. UC900 and CC900 showed a more varied response in both live cell counts and cellular viability relative to their non-degraded counterparts. In particular, UC900 had a significant decrease in live cell count (Fig. 5a), while no significant decreases in cellular viability were obtained for the thermally degraded clays, both relative to the control (Fig. 5b). CC900 displayed an increase in cellular proliferation at 72 h relative to 48 h and further confirmed the observed Region C changes in the α parameter. The ability of CC900 to display increased proliferation, may hint at its potential to produce effects similar to carcinogen carbon black; a complementary study noted for instance that carbon black caused an increase in epithelial cell proliferation, as well as increases in mutation frequency in these cells, therefore hinting at an increased prevalence of cancer incidence upon such exposures [74]. No significant differences were obtained between UC and UC900 and overall there were no major differences between sterilized and unsterilized nanoclays (Fig. S5a, b). Verma et al. complement our results on as received nanoclays by showing differences in toxicity in A549 cells based on the clay morphology, with platelet type nanoclays showing lower cell numbers relative to the tubular type, as well as varying toxicity between the platelet types [32].

To evaluate the last, namely whether changes in cell shape were correlated with the ECIS results, cellular imaging was used. Indeed, analysis showed that all of the clays and thermally degraded byproducts altered cellular shape and size, as well as cell confluence

(Fig. 6a–e). For instance, the exposed cells displayed abnormal cell shapes with a more stretched and altered profile away from the more oval shape of the control cells. Further, the membranes of the cells exposed to UC900 and CC900 did not appear as distinct as those of the control cells and further, the integrity of the exposed cell monolayer seemed compromised. Moreover, treatment with UC and CC caused significant decreases in the area of the cells relative to the control therefore further confirming the ECIS results (Fig. 6f); i.e., smaller cells would be taking up less room on the electrode, causing for more current to pass through and thus a lower resistance as shown by ECIS. Further, the dramatic loss of resistance and α shown for cells treated with CC along with the circular shape observed while imaging, show that alterations are likely occurring in cells' morphology as a first step towards cell transformation.

The larger effect observed for CC is presumably due to the presence of its organic modifier known to induce toxicity [30,31,35] through decreases in cellular proliferation [32], as well as membrane changes [29,33] and DNA damage [30,34,35]. It is our hypothesis that the route of the displayed toxicity of cells treated with CC could be through alteration of the cytoskeleton, causing for the observed decreases in resistance and α. Specifically, previous analysis for instance have shown that circular cells have lost their ability to attach to the substrate (electrode), as well as to other cells eventually leading to and/or serving as a signal of cell death [75,76]. Such changes in morphology are known to be occurring due to cytoskeleton reorganization [76] with alteration in cytoskeleton [44] leading to changes in cell mechanics [77], migration [78], differentiation [79], and organization [80]. While UC900 and CC900 did not experience as much a loss in the α parameter relative to the as received clays, they still showed decreases in resistance, possibly associated with reduced membrane integrity as observed in cellular imaging. Such changes in cell morphology, structure, and cell-substrate interactions may eventually lead to loss of cell-cell signaling [76,81].

Previously, the presence of the organic modifier in clays was associated to greater toxicity [29–31,35,82]. Janer et al. for instance tested dose-response (<500 μg/ml) of 5 cell lines and 1 primary cell line and found that clays organically modified with dimethyl dihydrogenated tallow ammonium and dimethyl benzyl hydrogenated tallow ammonium respectively had higher cytotoxicity relative to pristine clays [82]. When testing the modifier, quaternary ammonium compound (QAC), Sharma et al. found that the QAC had the same effect as the coated clay on the genotoxicity of Caco-2 cells, suggesting that the toxic effects were due to QAC [35]. Further, one study by Yoshida et al. found that organically modified silica particles coated with amine or carboxyl groups reduced the amount of reactive oxygen generation in HaCaT and TLR-1 cells. They also observed reduced DNA damage in HaCaT cells all relative to the unmodified silica particle, showing that the type of organic modifier and not just its presence plays a key role in toxicity [83].

While the full picture of the mechanistic toxicity of the nanoclays or end of life byproducts is still undergoing, to our knowledge, these are the first studies to identify toxicological profiles associated with cellular exposure to clay byproducts using a non-invasive and real-time cellular based platform. Further, while in our study we evaluated 4 different samples, one could envision creating a combinatorial assay to allow for profile identification based on

both sample as well as cellular characteristics thus extending the flexibility of this experimental set-up for toxicity evaluation of a large variety of nanomaterials, all in real-time and in a high-throughput fashion.

4. Conclusions

ECIS provided new means to identify the toxicity profiles of clays or byproducts, in a non-invasive, high-throughput, and real-time manner. Specifically, the morphological, behavioral, and viability changes observed in BEAS-2B cells after treatment with as received clay or thermally degraded byproducts show that such samples have the potential to produce toxic effects when used both in manufacturing or disposal environments. Organically modified nanoclay, CC, had the greatest toxic effects, with large losses in cell-substrate and cell-cell interactions and near maximal cell population loss by 72 h. Contrary, its thermally degraded byproduct, CC900, induced cell proliferation possibly hinting to similar toxic profiles to known carcinogen carbon black. UC, and its thermally degraded counterpart, UC900, displayed less significant toxic effects.

Supplementary Material

Refer to Web version on PubMed Central for supplementary material.

Acknowledgments

Appendix A. Supplementary data

Supplementary material is available on the material characterization and toxicity analyses of UV sterilized nanoclay and thermally degraded byproducts, sedimentation rates of the nanoclays and byproducts, and particle diameters as % volume determined via DLS. Supplementary data associated with this article can be found in the online version, at http://dx.doi.org/10.1016/j.bbagen.2016.09.003.

References

1. Roco MC. The long view of nanotechnology development: the National Nanotechnology Initiative at 10 years. J Nanopart Res. 2011; 13:427–445.

2. Sargent JF Jr. The National Nanotechnology Initiative: Overview, Reauthorization, and Appropriations Issues. Congressional Research Service. 2014

3. Paul DR, Robeson LM. Polymer nanotechnology: nanocomposites. Polymer. 2008; 49:3187–3204.

4. Singla P, Mehta R, Upadhyay SN. Clay modification by the use of organic cations. Green Sustain Chem. 2012; 2:21–25.

5. Ray SS, Okamoto M. Polymer/layered silicate nanocomposites: a review from preparation to processing. Prog Polym Sci. 2003; 28:1539–1641.

6. Ultracki LA, Sepehr M, Boccaleri E. Synthetic, layered nanoparticles for polymeric nanocomposites (PNCs). Polym Adv Technol. 2007; 18:1–37.

7. Floody MC, Theng BKG, Reyes P, Mora ML. Natural nanoclays: applications and future trends—a Chilean perspective. Clay Miner. 2009; 44:161–176.

8. Beall GW. The use of organo-clays in water treatment. Appl Clay Sci. 2003; 24:11–20.

9. Agarwal S, Tran P, Soong Y, Martello D, Gupta RK. Flow behavior of nanoparticles stabilized drilling fluids and effect of high temperature aging. J Pet Sci Eng. 2014; 117:15–27.

10. Jones TR. The properties and uses of clays which swell in organic solvents. Clay Miner. 1983; 18:399–410.

11. Elmore AR. Final report on the safety assessment of aluminum silicate, calcium silicate, magnesium aluminum silicate, magnesium silicate, magnesium trisilicate, sodium magnesium silicate, zirconium silicate, attapulgite, bentonite, Fuller's earth, hectorite, kaolin, lithium magnesium silicate, lithium magnesium sodium silicate, montmorillonite, pyrophyllite, and zeolite. Int J Toxicol. 2003; 22:37–102.

12. Tiwari RR, Khilar KC, Natarajan U. Synthesis and characterization of novel organomontmorillonites. Appl Clay Sci. 2008; 38:203–208.

13. Lebaron PC, Wang Z, Pinnavaia TJ. Polymer-layered silicate nanocomposites: an overview. Appl Clay Sci. 1999; 15:11–29.

14. Krikorian V, Pochan DJ. Poly (L-lactic acid)/layered silicate nanocomposite: fabrication, characterization, and properties. Chem Mater. 2003; 15:4317–4324.

15. Molinaro S, Romero MC, Boaro M, Sensidoni A, Lagazio C, Morris M, Kerry J. Effect of nanoclay-type and PLA optical purity on the characteristics of PLA-based nanocomposite films. J Food Eng. 2013; 117:113–123.

16. Zheng X, Wilkie CA. Flame retardancy of polystyrene nanocomposites based on an oligomeric organically-modified clay containing phosphate. Polym Degrad Stab. 2003; 81:539–550.

17. Choi R, Cheigh C, Lee S, Chung M. Preparation and properties of polypropylene/clay nanocomposites for food packaging. J Food Sci. 2011; 76:62–67.

18. Laufer G, Kirkland C, Cain AA, Grunlan JC. Oxygen barrier of multilayer thin films comprised of polysaccharides and clay. Carbohydr Polym. 2013; 95:299–302. [PubMed: 23618273]

19. Dalir H, Farahani RD, Nhim V, Samson B, Lévesque M, Therriault D. Preparation of highly exfoliated polyester-clay nanocomposites: process-property correlations. Langmuir. 2012; 28:791–803. [PubMed: 22087630]

20. Okada A, Usuki A. The chemistry of polymer-clay hybrids. Mater Sci Eng C. 1995; 3:109–115.

21. Barua S, Dutta N, Karmakar S, Chattopadhyay P, Aidew L, Buragohain AK, Karak N. Biocompatible high performance hyperbranched epoxy/clay nanocomposite as an implantable material. Biomed Mater. 2014; 9

22. Kevadiya BD, Thumbar RP, Rajput MM, Rajkumar S, Brambhatt H, Joshi GV, Dangi GP, Mody HM, Gadhia PK, Bajaj HC. Montmorillonite/poly-(e-caprolactone) composites as versatile layered material: reservoirs for anticancer drug and controlled release property. Eur J Pharm Sci. 2012; 47:265–272. [PubMed: 22525435]

23. Fogelström L, Malmström E, Johansson M, Hult A. Hard and flexible nanocomposite coatings using nanoclay-filled hyperbranched polymers. Appl Mater Interfaces. 2010; 2:1679–1684.

24. Meera KMS, Sankar RM, Murali A, Jaisankar SN, Mandal AB. Sol–gel network silica/modified montmorillonite clay hybrid nanocomposites for hydrophobic surface coatings. Colloids Surf. 2012; B 90:204–210.

25. Mitrano DM, Motellier S, Clavaguera S, Nowack B. Review of nanomaterial aging and transformations through the life cycle of nano-enhanced products. Environ Int. 2015; 77:132–147. [PubMed: 25705000]

26. Stern ST, McNeil SE. Nanotechnology safety concerns revisited. Toxicol Sci. 2008; 101:4–21. [PubMed: 17602205]

27. Dhawan A, Sharma V. Toxicity assessment of nanomaterials: methods and challenges. Anal Bioanal Chem. 2010; 398:589–605. [PubMed: 20652549]

28. Kroll A, Pillukat MH, Hahn D, Schnekenburger J. Current in vitro methods in nanoparticle risk assessment: limitations and challenges. Eur J Pharm Biopharm. 2009; 72:370–377. [PubMed: 18775492]

29. Lordan S, Kennedy JE, Higginbotham CL. Cytotoxic effects induced by unmodified and organically modified nanoclays in human hepatic HepG2 cell line. J Appl Toxicol. 2011; 31:27–35. [PubMed: 20677180]

30. Maisanaba S, Puerto M, Pichardo S, Jorda M, Moreno FJ, Aucejo S, Jos A. In vitro toxicological assessment of clays for their use in food packaging application, Food. Chem Toxicol. 2013; 57:266–275.

31. Maisanaba S, Gutièrrez-Praena D, Pichardo S, Moreno FJ, Jordá M, AM C, Aucejo S, Jos A. Toxic effects of a modified montmorillonite clay on the human intestinal cell line Caco-2. J Appl Toxicol. 2013; 34:714–725. [PubMed: 24122917]

32. Verma NK, Moore E, Blau W, Volkov Y, Babu PR. Cytotoxicity evaluation of nanoclays in human epithelial cell line A549 using high content screening and real-time impedance analysis. J Nanopart Res. 2012; 14

33. Baek M, Lee J, Choi S. Toxicological effects of cationic clay, montmorillonite in vitro and in vivo. Mol Cell Toxicol. 2012; 8:95–101.

34. Houtman J, Maisanaba S, Puerto M, Gutièrrez-Praena D, Jordá M, Aucejo S, Jos A. Toxicity assessment or organomodified clays used in food contact materials on human target cell lines. Appl Clay Sci. 2014; 90:150–158.

35. Sharma AK, Schmidt B, Frandsen H, Jacobsen NR, Larsen EH, Binderup M. Genotoxicity of unmodified and organo-modified montmorillonite. Mutat Res Genet Toxicol Environ Mutagen. 2010; 700:18–25.

36. Souza PMS, Morales AR, Marin-Morales MA, Mei LHI. PLA and montmorillonite nanocoposites: properties, biodegradation, and potential toxicity. J Polym Environ. 2013; 21:738–759.

37. Roes L, Patel MK, Worrell E, Ludwig C. Preliminary evaluation of risks related to waste incineration of polymer nanocomposites. Sci Total Environ. 2012; 417–418:76–86.

38. Lighty JS, Veranth JM, Sarofim AF. Combustion aerosols: factors governing their size and composition and implication to human health. J Air Waste Manage Assoc. 2000; 50:1565–1618.

39. Knirsch JM, Pulskamp K, Krug HF. Oops they did it again! Carbon nanotubes hoax scientists in viability assays. Nano Lett. 2006; 6:1261–1268. [PubMed: 16771591]

40. Monteiro-Riviere NA, Inman AO, Zhang LW. Limitations and relative utility of screening assays to assess engineering nanoparticle toxicity in a human cell line. Toxicol Appl Pharm. 2009; 234:222–235.

41. Casey A, Herzog E, Davoren M, Lyng FM, Byrne HJ, Chambers G. Spectroscopics analysis confirms the interactions between single walled carbon nanotubes and various dyes commonly used to assess cytotoxicity. Carbon. 2007; 45:1425–1432.

42. Hoet PH, Brüske-Hohlfeld I, Salata OV. Nanoparticles-known and unknown health risks. J Nanobiotechn. 2004; 2

43. Wang L, Zhu J, Deng C, Xing W, Cheng J. An automatic and quantitative on-chip cell migration assay using self-assembled monolayers combined with real-time cellular impedance sensing. Lab Chip. 2008; 8:872–878. [PubMed: 18497905]

44. Xi B, Yu N, Wang X, Xu X, Abassi YA. The application of cell-based label-free technology in drug discovery. Biotechn J. 2008; 3:484–495.

45. Xiao C, Lachance B, Sunahara G, Luong JHT. Assessment of cytotoxicity using electric cell-substrate impedance sensing: concentration and time response function approach. Anal Chem. 2002; 74:5748–5753. [PubMed: 12463358]

46. Giaever I, Keese CR. Micromotion of mammalian cells measured electrically. Proc Natl Acad Sci. 1991; 88:7896–7900. [PubMed: 1881923]

47. Wegener J, Keese CR, Giaever I. Electric cell-substrate impedance sensing (ECIS) as a noninvasive means to monitor the kinetics of cell spreading to artificial surfaces. Exp Cell Res. 2000; 259:158–166. [PubMed: 10942588]

48. Erdely A, Dahm M, Chen BT, Zeidler-Erdely PC, Fernback JE, Birch ME, Evans DE, Kashon ML, Deddens JA, Hulderman T, Bilgesu SA, Battelli L, Schwegler-Berry DE, Leonard HD, McKinney W, Frazer DG, Antonini JM, Porter DW, Castranova V, Schubauer-Berigan MK. Carbon nanotube dosimetry: from workplace exposure assessment to inhalation toxicology. Part Fibre Toxicol. 2013; 10

49. Hubbs A, Greskevitch M, Kuempel E, Fernando S, Toraason M. Abrasive blasting agents: designing studies to evaluate relative risk. J Toxicol Environ Health, Part A. 2005; 68:999–1016. [PubMed: 16020188]

50. Eldawud R, Stueckle TA, Manivanna S, Elbaz H, Chen M, Rojanasakul Y, Dinu CZ. Real-time analysis of the effects of toxic, therapeutic and sub-therapeutic concentrations of digitoxin on lung cancer cells. Biosens Bioelectron. 2014; 59:192–199. [PubMed: 24727605]

51. Yin LM, Wei Y, Wang Y, Xu YD, Yang YQ. Long term and standard incubations of WST-1 reagent reflect the same inhibitory trend of cell viability in rat airway smooth muscle cells. Int J Med Sci. 2013; 10:68–72. [PubMed: 23289007]

52. Zhang X, Rongjing X, Zenggang W, Zhou C. The synthesis and characterization of polyurethane/clay nanocomposites. Polym Int. 2003; 52:790–794.

53. Saikia BJ, Parthasarathy G. Fourier transform infrared spectroscopic characterization of kaolinite from Assam and Meghalay, northeastern India. J Mod Phys. 2010; 1:206–210.

54. Bishop J, Madejova J, Komadel P, Froschl H. The influence of structural, Fe, Al, and Mg on the infrared OH bands in spectra dioctahedral smectites. Clay Miner. 2001; 37:607–616.

55. Shameli K, Ahmad MB, Zargar M, Yunus W, Ibrahim NA, Shabanzadeh P, Moghaddam MG. Synthesis and characterization of silver/montmorillonite/chitosan bionanocomposites by chemical reduction method and their antibacterial activity. Int J Nanomedicine. 2011; 6:271–284. [PubMed: 21499424]

56. Xie W, Gao Z, Pan W, Hunter D, Singh A, Vata R. Thermal degradation chemistry of alkyl quaternary ammonium montmorillonite. Chem Mater. 2001; 13:2979–2990.

57. Rahimi-Razin S, Salami-Kalajahi M, Haddadi-Asl V, Roghani-Mamaqani H. Effect of different modified nanoclays on the kinetics of preparation and properties of polymer-based nanocomposites. J Polym Res. 2012; 19:1–16.

58. Ribeiro SPS, Estevao LRM, Nascimento RSV. Effect of clays on the fire-retardant properties of a polyethlenic copolymer containing intumescent formulation. Sci Techn Adv Mater. 2008; 9:1–7.

59. Kendall M, Hodges NJ, Whitwell H, Tyrrell J, Cangul H. Nanoparticle growth and surface chemistry changes in cell-conditioned culture medium. Philos Trans R Soc Lond B Biol Sci. 2015:370.

60. Lordan S, Higginbotham CL. Effect of serum concentration on the cytotoxicity of clay particles. Cell Biol Int. 2012; 36:57–61. [PubMed: 21883092]

61. Kuhlbusch TAJ, Asbach C, Fissan H, Göhler D, Stintz M. Nanoparticle exposure at nanotechnology workplaces: a review. Part Fibre Toxicol. 2011; 8

62. Jensen KA, Koponen IK, Clausen PA, Schneider T. Dustiness behaviour of loose and compacted bentonite and organoclay powders: what is the difference in exposure risk? J Nanopart Res. 2009; 11:133–146.

63. Tsai C, Huang C, Chen S, Ho C, Huang C, Chen C, Chang C, Tsai S, Ellenbecker MJ. Exposure assessment of nano-sized and respirable particles at different workplaces. J Nanopart Res. 2011; 13:4161–4172.

64. Kim W, Lee DW, Lee S. Size characterization of incinerator fly ash using sedimentation/steric field-flow fractionation. Anal Chem. 2002; 74

65. Chang F, Wey M. Comparison of the characteristics of bottom and fly ashes generated from various incineration processes. J Hazard Mater. 2006; B138:594–603.

66. Siegrist KJ, Reynolds SH, Kashon ML, Lowry DT, Dong C, Hubbs AF, Young S, Salisbury JL, Porter DW, Benkovic SA, McCawley M, Keane MJ, Mastovich JT, Bunker KL, Gena LG, Sparrow MC, Sturgeon JL, Dinu CZ, Sargent LM. Genotoxicity of multi-walled carbon nanotubes at occupationally relevant doses. Part Fibre Toxicol. 2014; 11

67. Schinwald A, Murphy FA, Jones A, MacNee W, Donaldson K. Graphene-based Nanoplatelets: a new risk to the respiratory system as a consequence of their unusual aerodynamic properties. ACS Nano. 2012; 6:736–746. [PubMed: 22195731]

68. Gangwal S, Brown JS, Wang A, Houck KA, Dix DJ, Kavlock RJ, Cohen Hubal EA. Informing selection of nanomaterial concentration for ToxCast in vitro testing based on occupational exposure potential. Environ Health Perspect. 2011; 119:1539–1546. [PubMed: 21788197]

69. Benson K, Cramer S, Galla H. Impedance-based Cell Monitoring: Barrier Properties and Beyond. Fluids and Barriers of the CNS. 2013; 10:1–11. [PubMed: 23305147]

70. Arndt S, Seebach J, Psathaki K, Galla H, Wegener J. Bioelectrical impedance assay to monitor changes in cell shape during apoptosis. Biosens Bioelectron. 2004; 19:583–594. [PubMed: 14683642]

71. Xiao C, Luong JHT. Assessment of cytotoxicity by emerging impedance spectroscopy. Toxicol Appl Pharm. 2005; 206:102–112.

72. Male KB, Lachance B, Hrapovic S, Sunahara G, Luong JHT. Assessment of cytotoxicity of quantum dots and gold nanoparticles using cell-based impedance spectroscopy. Anal Chem. 2008; 80:5487–5493. [PubMed: 18553941]

73. Lo C, Keese CR, Giaever I. Impedance analysis of MDCK cells measured by electric cell-substrate impedance sensing. Biophys J. 1995; 69:2800–2807. [PubMed: 8599686]

74. Driscoll KE, Carter JM, Howard BW, Hassenbein DG, Pepelko W, Baggs RB, G O. Pulmonary inflammatory, chemokine, and mutagenic responses in rats after subchronic inhalation of carbon black. Toxicol Appl Pharmacol. 1996; 136:372–380. [PubMed: 8619246]

75. Frisch SM, Francis H. Disruption of Epithelial Cell-Matrix Interactions Induces Apoptosis. J Cell Biol. 124:619–626.

76. Re F, Zanetti A, Sironi M, Polentarutti N, Lanfrancone L, Dejana E, Colotta F. Inhibition of anchorage-dependent cell spreading triggers apoptosis in cultured human endothelial cells. J Cell Biol. 1994; 127:537–546. [PubMed: 7523422]

77. Dong C, Kashon ML, Lowry DT, Dordick JS, Reynolds SH, Rojanasakul Y, Sargent LM, Dinu CZ. Exposure to carbon nanotubes leads to changes in the cellular biomechanics. Adv Healthcare Mater. 2013; 2:1–7.

78. Shen Y, Leng M, Yu H, Zhang Q, Luo X, Gregersen H, Wang G, Liu X. Effect of amphiphilic PCL-PEG nano-micelles on HEpG2 cell migration. Macromol Biosci. 2015; 15:372–384. [PubMed: 25367414]

79. Zou J, Wang X, Zhang L, Wang J. Iron nanoparticles significantly affect the in vitro and in vivo expression of *Id* genes. Chem Res Toxicol. 2014

80. Zhou X, Wang B, Chen Y, Mao Z, Gao C. Uptake of cerium oxide nanoparticles and their influences on functions of A549 cells. J Nanosci Nanotechn. 2013; 13:204–215.

81. Hussain S, Thomassen LCJ, Ferecatu I, Borot M, Andreau K, Martens JA, Fleury J, Baeza-Squiban A, Marano F, Boland S. Carbon black and titanium dioxide nanoparticles elicit distinct apoptotic pathways in bronchial epithelial cells. Part Fibre Toxicol. 2010; 7

82. Janer G, Fernández-Rosas E, del Molino E Mas, González-Gáalvez D, Vilar G, López-Iglesias C, Ermini V, Vázquez-Campos S. In vitro toxicity of functionalised nanoclays is mainly driven by the presence of organic modifier. Nanotoxicology. 2014; 8:279–294. [PubMed: 23405880]

83. Yoshida T, Yoshioka Y, Matsuyama K, Nakazato Y, Tochigi S, Hirai T, Kondoh S, Nagano K, Abe Y, Kamada H, Tsunoda S, Nabeshi H, Yoshikawa T, Tsutsumi Y. Surface modification of amorphous nanosilica particles suppresses nanosilica-induced cytotoxicity, ROS generation, and DNA damage in various mammalian cells. Biochem Biophys Res Commun. 2012; 427:748–752. [PubMed: 23044420]
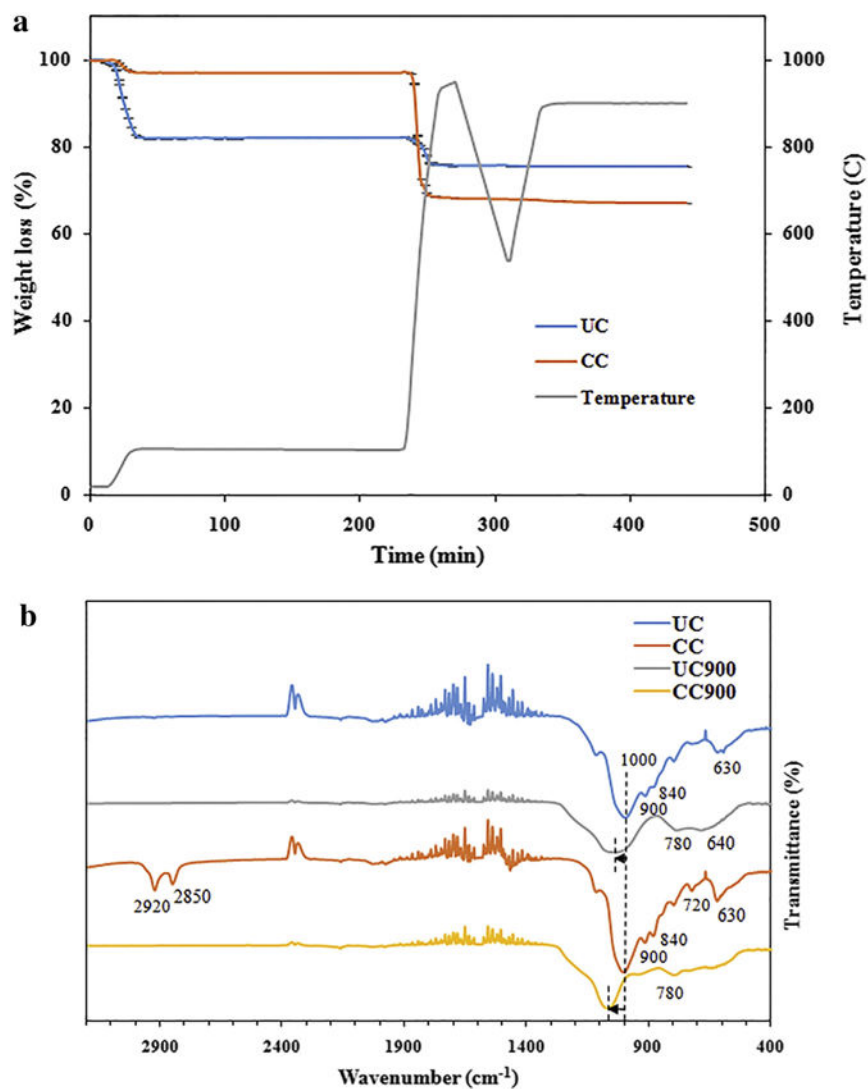
Fig. 1.
(a) Thermal degradation profile of UC and CC (n = 2). (b) FTIR spectrum for UC and CC along with their thermally degraded byproducts (n = 2).
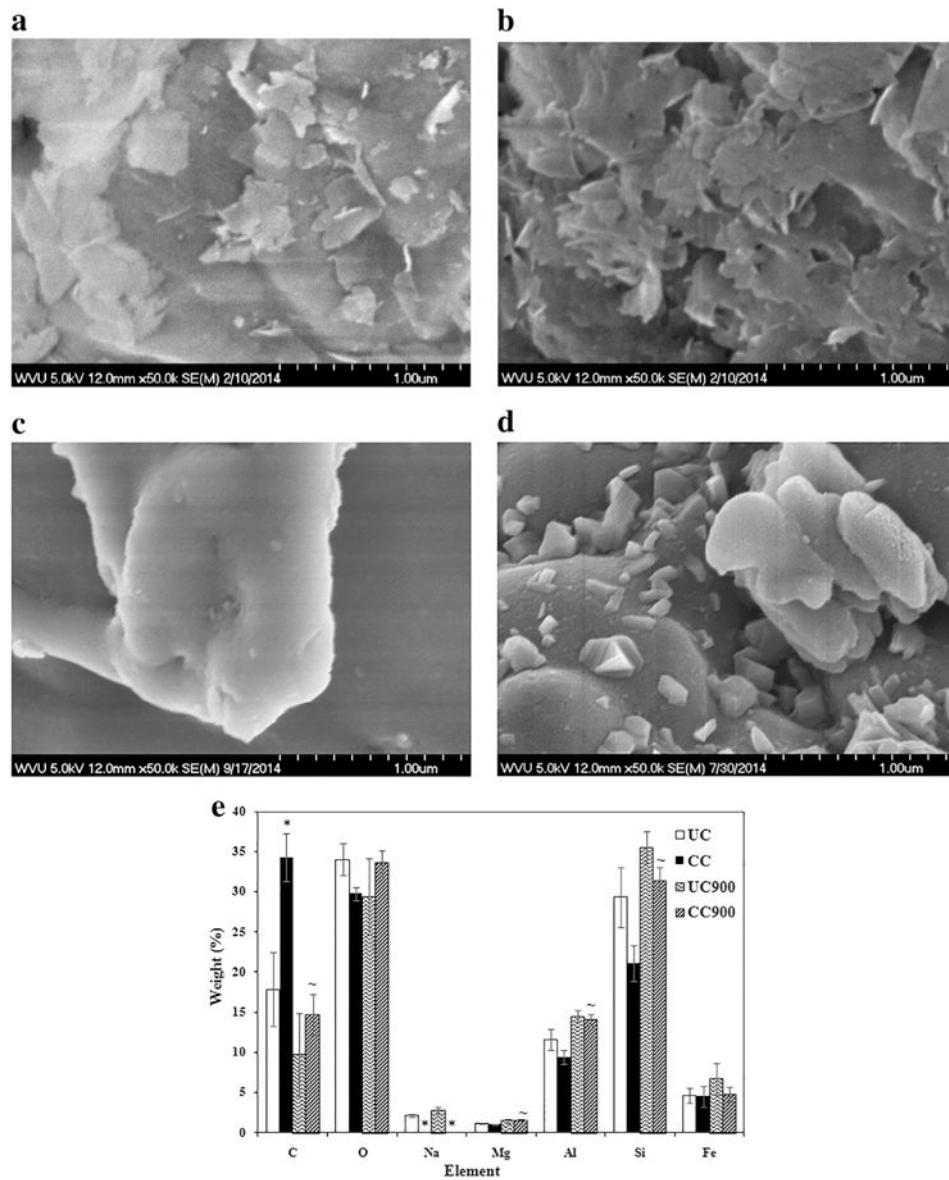
Fig. 2.
Surface morphology of (a) UC, (b) CC, and thermally degraded (c) UC900, and (d) CC900 as determined by SEM. (e) Elemental composition of as received nanoclay and their thermally degraded byproducts as determined by EDX at 1 μm (n = 5). The symbols * and ~ indicate significant differences between UC and CC and between as received nanoclay and its thermally degraded byproduct, respectively.
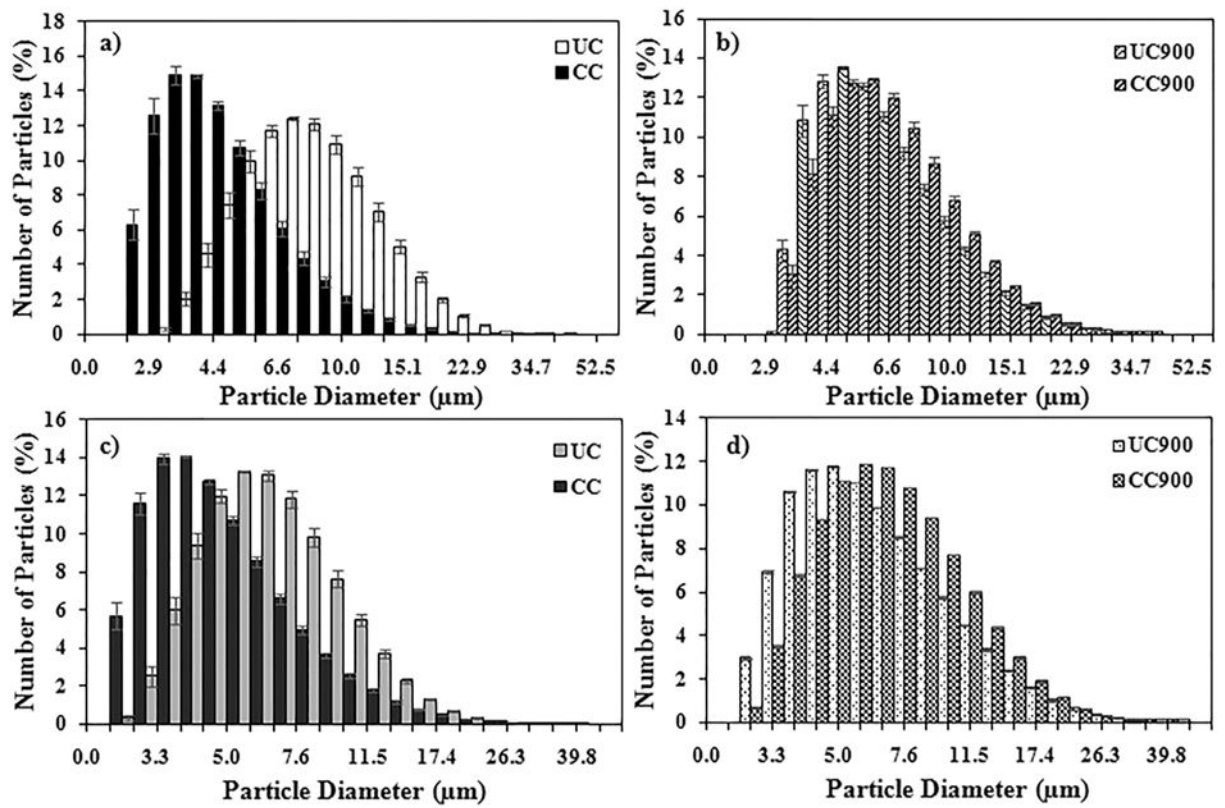
Fig. 3.
Average particle diameter size distribution of UC, CC, UC900, and CC900 in solutions of (a and b) media or (c and d) PBS.
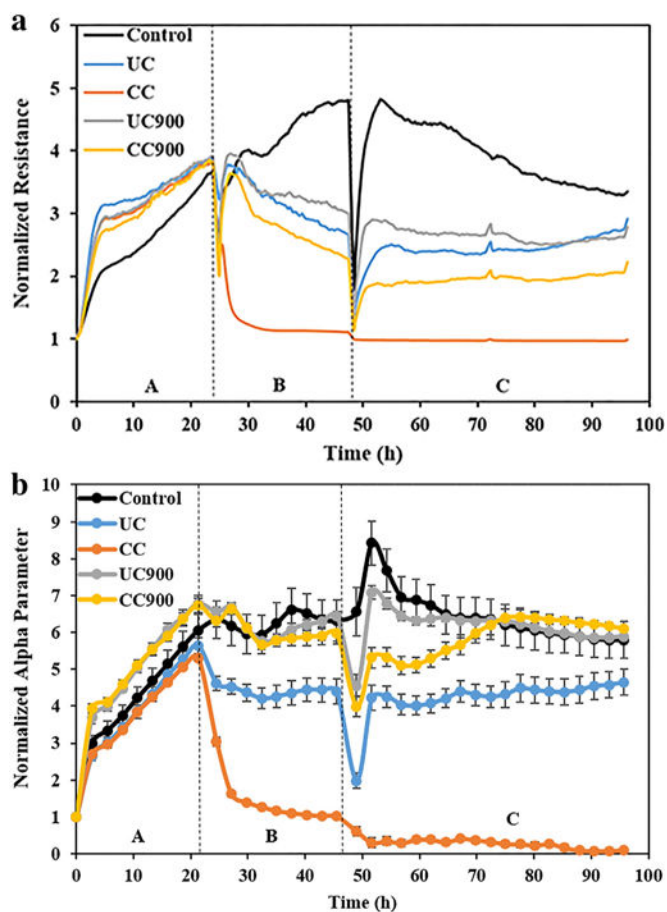
Fig. 4.
(a) Representative real-time measurements of normalized resistance for BEAS-2B cells before (Region A), during (Region B), and after treatment (Region C) with as received and thermally degraded nanoclays. (b) Real-time measurements of normalized alpha (α) parameter for BEAS-2B cells before (Region A), during (Region B), and after treatment (Region C) with as received and thermally degraded nanoclays.
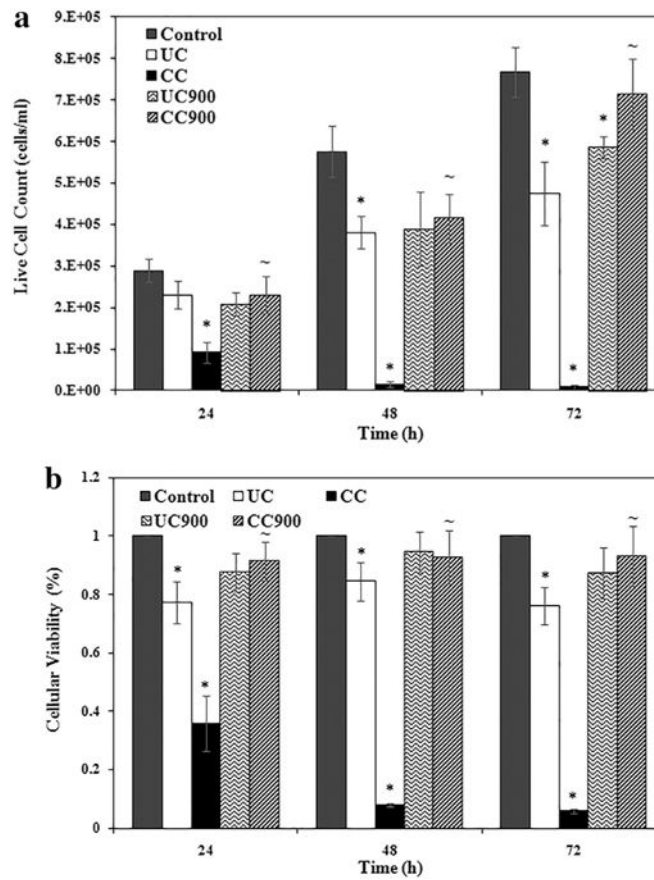
Fig. 5.
Toxicity of as-received and thermally degraded nanoclays determined by (a) live cell count and (b) cellular viability via WST assay, for unsterilized nanoclay (n = 6). The symbols * and ~ indicate significant differences between the control and nanoclay treatments and between as received nanoclay and thermally degraded byproducts, respectively.
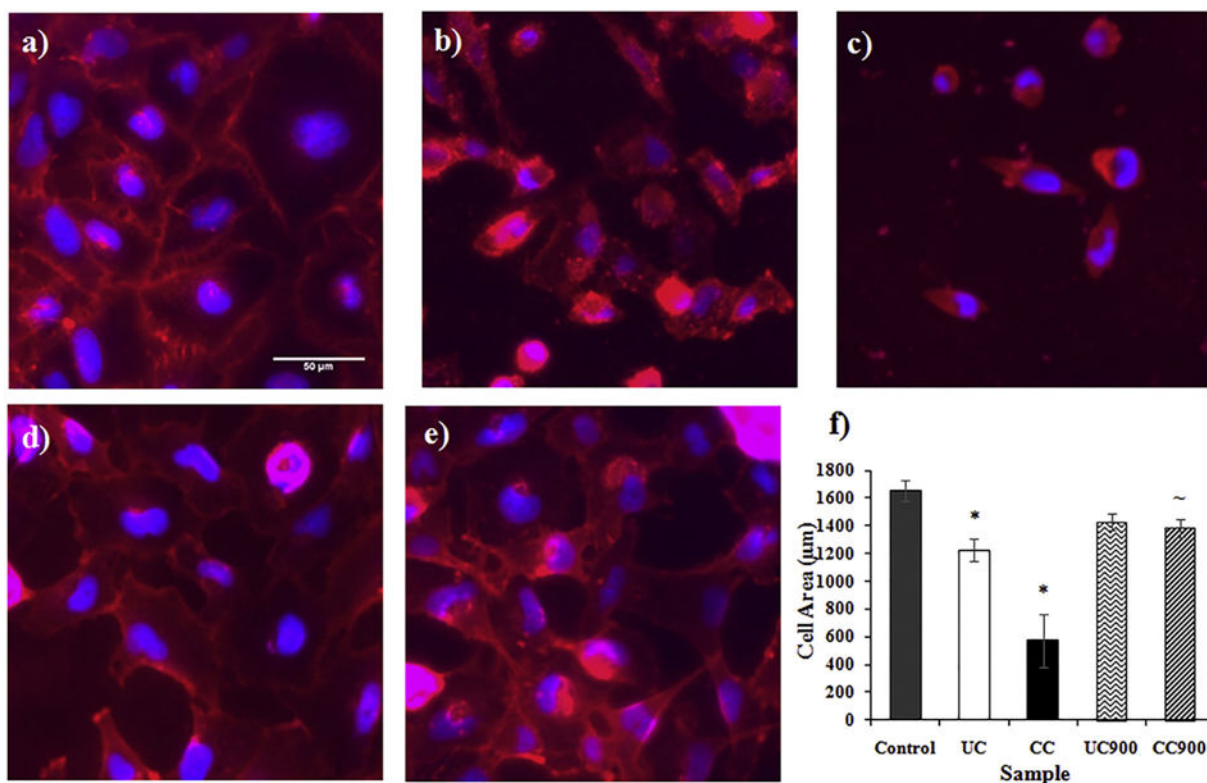
Fig. 6.
Fluorescent images of the cell membrane (red) and nucleus (blue) for (a) control cells and cells treated with (b) UC, (c) CC, (d) UC900, and (e) CC900 after 24 h. (f) Cell area (μm) after 24 h of treatment with nanoclays (n = 3). The symbols * and ~ indicate significant differences between the control and nanoclay treatments and between as received nanoclay and thermally degraded byproducts, respectively.

Table 1

Amount of moisture, volatile, ash, and fixed carbon present in UC and CC as determined by TGA.

	Moisture (%)	Volatile (%)	Ash (%)	Fixed carbon (%)
UC	17.76 ± 0.12	6.31 ± 0.04	75.72 ± 0.13	0.22 ± 0.03
CC	2.81 ± 0.01*	28.87 ± 0.01*	67.28 ± 0.01*	1.05 ± 0.00*

The symbol * indicates a significant difference between UC and CC.

Table 2

Average particle diameter distribution sizes (µm) in solutions of media relative to the number of particles.

	UC	CC	UC900	CC900
<10%	4.66 ± 0.25	2.63 ± 0.06	3.58 ± 0.08	3.75 ± 0.13
<50%	7.70 ± 0.40	3.85 ± 0.17	5.50 ± 0.18	5.89 ± 0.23
<90%	13.91 ± 0.48	7.23 ± 0.36	10.86 ± 0.24	11.22 ± 0.29

Table 3

Average particle diameter distribution sizes (μm) in solutions of PBS relative to the number of particles.

	UC	CC	UC900	CC900
<10%	3.88 ± 0.16	2.66 ± 0.06	3.32 ± 0.01	3.75 ± 0.01
<50%	6.16 ± 0.26	3.99 ± 0.12	5.41 ± 0.02	6.23 ± 0.00
<90%	11.02 ± 0.30	7.86 ± 0.23	11.28 ± 0.04	11.88 ± 0.02